JES Focus Issue on Mathematical Modeling of Electrochemical Systems at Multiple Scales in Honor of John Newman

Numerical Solution of Moving Phase Boundary and Diffusion-Induced Stress of Sn Anode in the Lithium-Ion Battery

Chun-Hao Chen,[z] Eric Chason,[z] and Pradeep R. Guduru[z]

School of Engineering, Brown University, Providence, Rhode Island 02912, USA

We have previously observed a large transient stress in Sn film anodes at the beginning of the Sn-Li_2Sn_5 phase transformation. To understand this behavior, we use numerical modeling to simulate the kinetics of the 1-D moving boundary and Li diffusion in the Sn anodes. A mixture of diffusion-controlled and interface-controlled kinetics is found. The Li concentration in the Li_2Sn_5 phase remains near a steady-state profile as the phase boundary propagates, whereas the Li diffusion in Sn is more complicated. Li continuously diffuses into the Sn layer and produces a supersaturation; the Li can then diffuse toward the Sn/Li_2Sn_5 interface and contribute to further phase transformation. The evolution of Li concentration in the Sn induces strain which involves rate-dependent plasticity and elastic unloading, resulting in the complex stress evolution that is observed. In the long term, the measured stress is dominated by the stress in the growing Li_2Sn_5 phase.

Manuscript submitted April 3, 2017; revised manuscript received July 19, 2017. Published August 2, 2017. *This paper is part of the JES Focus Issue on Mathematical Modeling of Electrochemical Systems at Multiple Scales in Honor of John Newman.*

Sn electrodes have a large theoretical capacity (994 mAh/g)[1] which makes them a promising anode material for Li-ion batteries. However, during lithiation/delithiation, Sn reacts with Li and forms multiple lithiated phases at different states of charge. The large volumetric changes (~300%) associated with the phase transformations induce capacity loss through mechanical degradation, which provides motivation for understanding the strain relaxation processes in the material. In a previous publication,[2] we reported potentiostatic experiments of the initial lithiation of Sn anodes in which the original Sn phase transforms into the first lithiated phase Li_2Sn_5. In-situ curvature measurements of the thin film samples were performed during the lithiation to monitor the stress and we observed a transient behavior in the initial stages of the phase transformation. The curvature measurement (Fig. 1) shows that a high stress state occurs at the beginning of the phase transformation which then rapidly decreases followed by steady-state behavior. Understanding the origin of this transient behavior and its implication for rate-dependent plastic deformation in the layer is the focus of this work.

Diffusion-induced stress has been studied previously in Li-ion battery research to understand mechanical failures of electrodes. Bower and Guduru[3] performed a finite element model of diffusion and plasticity in amorphous Si electrodes. Zhang et al.[4] studied graphite anodes with a layered structure. Christensen[5] presented a mathematical model of the particles in porous lithium manganese oxide cathodes and graphite-based anodes. These works primarily focused on the stress distribution in a single phase region which has a concentration gradient. In contrast, the transient behavior in the experiments that are the subject of this work was observed at the beginning of the phase transformation where the phase boundary propagated along with diffusion in both the Sn and Li_2Sn_5 layers. The resulting concentration profile and interface motion must be analyzed in terms of a moving boundary problem, a classical problem in solid state diffusion. A class of literature has been published on solving the moving boundary of the heat transfer problem, so called Stephan problem.[6,7] In Li-ion battery research, phase transformations in crystalline-Si[8] electrode and cathode materials[9] have also been studied. Hulikal et al.[10] have performed phase-field modeling on phase transformation of Sn electrode.

The concentration in a moving boundary value problem does not have a simple analytical solution. Therefore, in this work we have performed a numerical solution to simulate the evolution of the phase boundary and Li concentration in the Sn and Li_2Sn_5 layers during potentiostatic lithiation. At the same time, we use a model of diffusion-induced stress with rate-dependent plasticity and elastic unloading to analyze the corresponding curvature measurements.

Experimental

Electrochemical experiments on Sn thin-film electrode.—The experiments were performed in a customized electrochemical half cell (shown in Fig. 2) with 1.5 mm-thick (50.8 mm in diameter) lithium metal foil used as both the reference and counter electrode and an electroplated thin film of Sn as the working electrode. The electrolyte was 1.2 M $LiPF_6$ in ethylene carbonate (EC):diethyl carbonate (DEC) (1:2 by wt%) solvent. Sn films with thickness of 1.85 μm were electroplated on a fused-silica substrates (thickness of 500 μm) with evaporated Cu (50 nm) and Ti (25 nm) layers. Further details of the sample fabrication have been described in the previous report.[2] The cells were built and operated in an Ar-filled glove box. In order to distinguish the charge consumed by SEI formation and lithiation as much as possible, the anodes were first processed to grow a SEI layer at 0.8 V vs. Li/Li^+ for 20 hours before growth of the lithiated Sn phase. After the SEI growth, potentiostatic lithiation was performed at a selective potential (0.65 V) below the potential plateau of Li_2Sn_5 (0.76 V[11]) to activate the Sn-Li_2Sn_5 phase transformation. The potential was kept high enough to not activate the formation of other more highly lithiated phases. The potentiostatic lithiation was performed for approximately 100 hours. The measured current density evolution is shown in Fig. 1a.

In-situ curvature measurement.—During the electrochemical treatments, wafer curvature measurements using the Multi-Beam Optical Stress Sensor (MOSS) technique (k-Space Associates) were performed to determine the stress evolution. The setup (shown in Fig. 2) monitors an array of laser beams that are reflected from the backside of the substrate into a charge-coupled device (CCD) camera. The curvature is determined by measuring the change in spacing between the reflected beams. The measured curvature ($1/R$) is related to the average film stress $\langle\sigma\rangle$ by Stoney's equation,

$$\langle\sigma\rangle h_f = \frac{M_s h_s^2}{6}\frac{1}{R} \quad [1]$$

where h_f and h_S are the thicknesses of the film and the substrate, respectively. M_S is the biaxial modulus of the substrate. The product $\langle\sigma\rangle h_f$ is called the stress-thickness and can be obtained from the curvature data using Eq. 1. As seen in the previous publication,

[z]E-mail: chun-hao_chen@alumni.brown.edu; eric_chason@brown.edu; pradeep_guduru@brown.edu

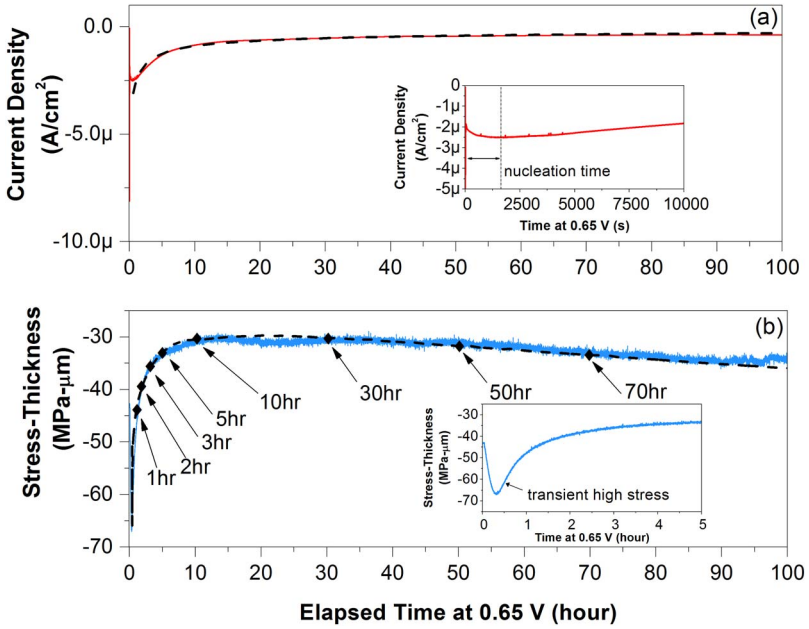

Figure 1. Measurements and calculations (dashed lines) during the potentiostatic lithiation experiments at 0.65 V. (a) current density and inset showing the nucleation time; (b) stress-thickness and inset showing the transient high stress state. Arrows indicate the times used for calculations of the profiles discussed in text and shown in Figs. 7, 8 and 10.

the Sn/Li_2Sn_5 interface remains fairly planar during propagation, so we consider the experiments as a 1-D problem with multiple layers. Therefore, the measured stress-thickness is due to contributions from each layer:

$$\langle\sigma\rangle h_f = \langle\sigma_{SEI}\rangle h_{SEI} + \langle\sigma_{Sn}\rangle h_{Sn} + \langle\sigma_{Li_2Sn_5}\rangle h_{Li_2Sn_5} \qquad [2]$$

where the subscripts indicate the stress and thickness in the SEI, Sn and Li_2Sn_5 layers. This analysis assumes that the layers can be treated as uniform in thickness and state of stress in the lateral direction.

Modeling and Calibration

To understand the transient behavior observed in the curvature measurements, we developed a kinetic model to simulate the phase evolution and utilized the experimental results to extract the relevant kinetic and mechanical parameters. We assume that during potentiostatic lithiation, the Li concentration at the surface is established by the applied potential and remains constant during the experiment. The phase transformation is initiated by lowering the applied potential and then proceeds in two stages. In the first stage, the Li_2Sn_5 phase nucleates and grows near the surface of the anode, resulting in a continuous layer. Subsequently, the Sn/Li_2Sn_5 phase boundary propagates in the anode as the Sn layer is continuously transformed into the Li_2Sn_5 phase. In the following sections, we discuss a continuum model for the Li concentration profile, layer stress and phase boundary propagation in the two stages. The finite-difference method is used to solve the model and the results are compared with the experimental results.

Kinetic model in the nucleation stage.—As the applied potential is changed to a value below the threshold for the phase transformation, a higher Li concentration is established at the surface that activates the nucleation of the Li_2Sn_5 phase (β phase). We assume the nucleation happens in a thin region near the surface of the anode. In the nucleation region (thickness of S_o), the nuclei form and grow while some Li also diffuses into the Sn (α phase). A schematic plot of the Li concentration is shown in the inset of Fig. 3. The Li concentration at the Sn/Li_2Sn_5 phase boundary in the Sn phase ($x = S_o$) is assumed to remain at the equilibrium concentration, $C^{eq}_{\alpha\beta}$, i.e. the Li solubility in Sn phase. The substrate is assumed to be impervious to Li.

The concentration of accumulated Li in the Sn phase during the nucleation period can be obtained by solving a 1-D diffusion. The governing equation and boundary conditions for the diffusion in Sn are:

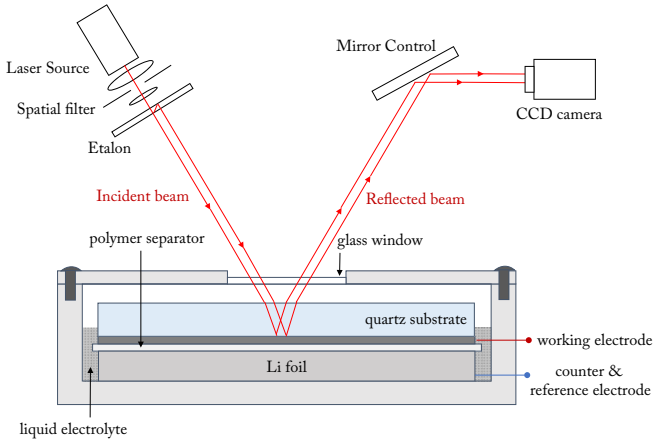

Figure 2. Schematic of electrochemical half cell and in-situ curvature measurement (MOSS).

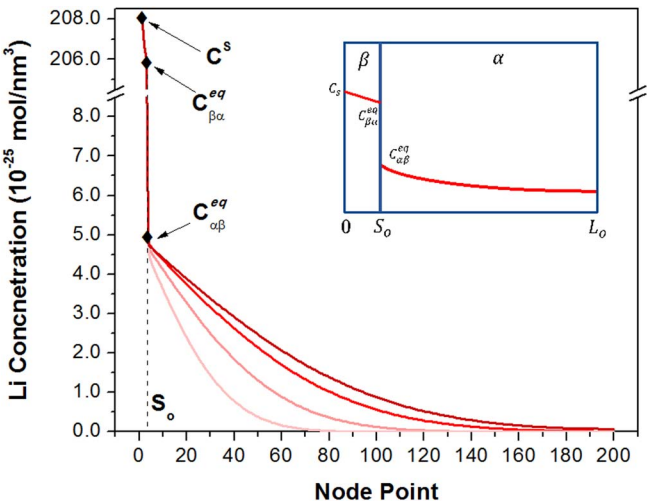

Figure 3. Schematic plot and calculated Li concentration for the initial nucleation stage of the numerical simulations.

- Governing Equation

$$\frac{\partial C_\alpha(x,t)}{\partial t} = D_\alpha \frac{\partial^2 C_\alpha(x,t)}{\partial x^2}, \text{ for Sn region, } S_0 \le x \le L_0 \quad [3]$$

- Boundary Conditions

$$C_\alpha(S_o,t) = C_{\alpha\beta}^{eq}; \frac{\partial C_\alpha(L_0,t)}{\partial x} = 0 \quad [4]$$

L_0 is the original thickness of the Sn anode and D_α is the Li diffusivity in Sn. Normalized forms of the position $\xi = x/L_0$, time $\tau = D_\alpha t/L_0^2$, and concentration of Li $\theta = (C_\alpha - C_{\alpha\beta}^{eq})/(C_i - C_{\alpha\beta}^{eq})$ are used in solving the equations, where C_i is the initial Li concentration in Sn. Note that θ is defined such that it starts from a value of 1 and approaches 0 as C_α reaches $C_{\alpha\beta}^{eq}$. The analytical solution of the concentration profile is

$$\theta(\xi,\tau) = \sum_{n=0}^{\infty} \frac{4}{(2n+1)\pi} \frac{\sin(2n+1)\pi\xi}{2} e^{\frac{-(2n+1)^2\pi^2}{4}\tau} \quad [5]$$

Eq. 5 provides the concentration profile of Li in Sn established during a given nucleation time t_o, and it is used in the second stage of the numerical solution as the initial Li concentration profile in the Sn phase. The evolution of Li concentration in Sn during nucleation obtained by Eq. 5 is shown in Fig. 3. For the profile inside the nucleation region, we assume the Li diffusion is fast so the concentration at the phase boundary is at the equilibrium concentration $C_{\beta\alpha}^{eq}$ i.e. the stoichiometric Li concentration of Li_2Sn_5 phase. Therefore, a linear Li concentration profile is assumed with the surface concentration C_s and $C_{\beta\alpha}^{eq}$ at the phase boundary.

Kinetic model with a moving phase boundary.—When the nucleation of the new phase is completed, the individual Li_2Sn_5 nuclei coalesce to form a continuous layer at the surface of the anode. At this point, we assume there is a stable Sn/Li_2Sn_5 phase boundary at $x = S_0$. Subsequently, many of the Li atoms that enter the electrode are consumed in advancing the phase boundary into the Sn layer by the growth of the lithiated phase. However, if the boundary does not move rapidly enough then there can be diffusion of excess Li into the Sn phase. On the other hand, if there is excess Li in the Sn layer (i.e. above the solubility limit) then it can also diffuse to the Sn/Li_2Sn_5 interface and contribute to further Li_2Sn_5 phase growth. Therefore, the kinetic model described here includes diffusion in both Sn and Li_2Sn_5 layers and a moving phase boundary driven by fluxes of Li from both directions. The governing equations and boundary conditions are:

- Governing Equations:

$$\frac{\partial C_\beta(x,t)}{\partial t} = D_\beta \frac{\partial^2 C_\beta(x,t)}{\partial x^2}, \text{ for } Li_2Sn_5 \text{ (}\beta\text{ phase)}, 0 \le x \le S(t) \quad [g1]$$

$$\frac{\partial C_\alpha(x,t)}{\partial t} = D_\alpha \frac{\partial^2 C_\alpha(x,t)}{\partial x^2}, \text{ for Sn (}\alpha\text{ phase)}, S(t) \le x \le L(t) \quad [g2]$$

$$D_\beta \frac{\partial C_\beta^{S^-}}{\partial x} - D_\alpha \frac{\partial C_\alpha^{S^+}}{\partial x} = \left(C_\alpha^{S^+} - C_\beta^{S^-}\right) \frac{dS(t)}{dt} \quad [g3]$$

- Boundary Conditions:

$$C_\beta(0,t) = C_s \quad [b1]$$

$$\frac{\partial C_\alpha(L(t),t)}{\partial x} = 0 \quad [b2]$$

$$C_\alpha^{S^+} = C_{\alpha\beta}^{eq} + \left[C_\beta^{S^-} - C_{\beta\alpha}^{eq}\right] \quad [b3]$$

$$\frac{dS(t)}{dt} = K\left(C_\beta^{S^-} - C_{\beta\alpha}^{eq}\right) \quad [b4]$$

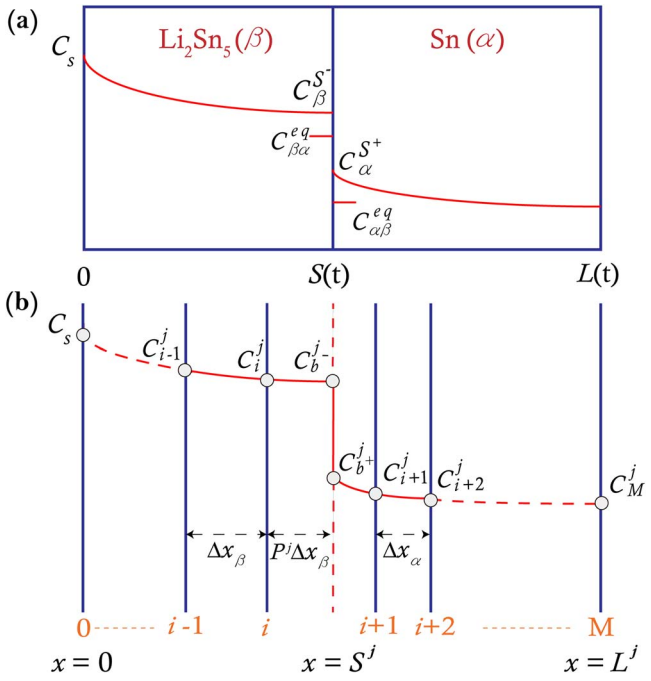

Figure 4. Schematic plot of (a) concentration profiles in kinetic model and (b) corresponding numerical simulation framework of the moving boundary.

A schematic plot of the kinetic model is shown in Fig. 4. The range of x is defined as $0 \le x \le L(t)$, where $x = 0$, is the electrolyte/anode interface and $x = L(t)$ is the anode/substrate interface. Note that $L(t)$ is a function of time due to the volume expansion caused by the phase transformation. The anode is divided into two regions by the phase boundary; Sn (α phase) for $x \ge S(t)$ and Li_2Sn_5 (β phase) for $x \le S(t)$. We assume the diffusion of Li atoms to be described by Fick's law as shown in governing Equations g1 and g2. D_α and D_β are the diffusion coefficients of Li in Sn and Li_2Sn_5 respectively, and are assumed to be constant. The Stephan condition of the phase boundary movement is shown in governing Equation g3. $C_\alpha^{S^+}$ and $C_\beta^{S^-}$ denote the Li concentrations at the Sn/Li_2Sn_5 phase boundary in Sn phase and in Li_2Sn_5 phase respectively. $\frac{dS(t)}{dt}$ is the velocity of the Sn/Li_2Sn_5 phase boundary.

The boundary conditions given in b1–b4 are chosen to agree with the experimental conditions. In our model, we neglect the effect of SEI on the electrochemical processes at the electrolyte/anode interface. We assume that a constant cell potential under potentiostatic condition corresponds to a constant Li concentration C_S at $x = 0$. In boundary condition (b2), we assume the substrate to be impervious to Li, so the Li flux at the anode/substrate interface is set to zero. At equilibrium, the chemical potentials on both sides of the interface are the same, i.e. $\mu_{\alpha,Li}^{eq} = \mu_{\beta,Li}^{eq}$, and the corresponding equilibrium concentrations are the Li solubility of the Sn phase $C_{\alpha\beta}^{eq}$ and the stoichiometric concentration of the Li_2Sn_5 phase $C_{\beta\alpha}^{eq}$. During the phase boundary propagation, the actual chemical potentials on either side of the phase boundary are expected to deviate from the equilibrium values. In general, the chemical potential can be discontinuous across a moving phase boundary, although it is often assumed that they are equal in the literature.[12] Here, we allow them to be discontinuous with a drop of $\Delta\mu$ across the interface.[13]

$$\Delta\mu = \mu_{\beta,Li} - \mu_{\alpha,Li} \quad [6]$$

where $\mu_{\alpha,Li}$ and $\mu_{\beta,Li}$ are chemical potentials on Sn and Li_2Sn_5 sides of the interface respectively. The chemical potential difference can be represented as

$$\Delta\mu = \mu_{\beta,Li}^{eq} + kT \ln \gamma_\beta \delta C_{\beta,Li} - \mu_{\alpha,Li}^{eq} - kT \ln \gamma_\alpha \delta C_{\alpha,Li} \quad [7]$$

where γ_α and γ_β are activity coefficients and the logarithmic terms include the deviations of the chemical potential from the equilibrium values ($\delta C_{\alpha,Li} = C_\alpha^{S^+} - C_{\alpha\beta}^{eq}$ and $\delta C_{\beta,Li} = C_\beta^{S^-} - C_{\beta\alpha}^{eq}$). The equilibrium chemical potentials can be eliminated and by rearranging Eq. 7, the remaining terms lead to

$$\frac{\gamma_\alpha}{\gamma_\beta} exp\left(\frac{\Delta\mu}{kT}\right) = \frac{\delta C_{\beta,Li}}{\delta C_{\alpha,Li}} = \frac{C_\beta^{S^-} - C_{\beta\alpha}^{eq}}{C_\alpha^{S^+} - C_{\alpha\beta}^{eq}}. \quad [8]$$

According to the Li-Sn phase diagram,[14] both the Sn and Li_2Sn_5 phase have limited Li solubility, so we assume that the non-ideal behavior of Li in both phase are similar and the ratio of activity coefficients $\frac{\gamma_\alpha}{\gamma_\beta}$ is close to 1. In addition, the chemical potential drop $\Delta\mu$ at the interface is considered to be small by assuming the Li diffusion across the interface is fast and the interface is negligibly thin as used in the literature.[15] Therefore, we assume the product $\frac{\gamma_\alpha}{\gamma_\beta} exp(\frac{\Delta\mu}{kT})$ is approximated to be 1, and Eq. 8 leads to the boundary condition (b3). The Li concentration in both layers are higher than the equilibrium values, which means that only the diffusion of excess Li atoms in Sn and Li_2Sn_5 are considered here.

The deviation from the equilibrium state induces a supersaturation of Li at the phase boundary which is the driving force for the phase boundary movement as represented in boundary condition (b4). K is the reaction rate coefficient for the Sn-Li_2Sn_5 phase transformation, a measure of the mobility of the phase boundary. For larger values of K, the phase boundary propagates more rapidly for a specific value of the supersaturation. If $K \to \infty$, the phase boundary movement depends only on the diffusion in the layers, which is referred to as the diffusion-controlled case. In the limit where $K \to 0$, the phase boundary movement is determined by the reaction rate of phase transformation at the interface, which is the interface-controlled case. In intermediate situations, the kinetics are 'mixed.' In the current kinetic picture, with a finite value of K, the phase propagation is determined by both diffusion in the phases and the reaction at the interface.

Numerical solution of the moving boundary problem.—Moving boundary problems have been solved by a variety of methods in the literature.[8,16–22] Here, we use the finite-difference method with a solution technique developed by Crank.[23] This involves a front-tracking method with a fixed grid that spans the entire simulated domain. The grid spacing is allowed to be different in each phase to accommodate volume expansion. The whole region is subdivided into M intervals. The mesh size in the Sn region is $\Delta x_\alpha = L_o/M$, and the mesh size in the Li_2Sn_5 phase is $\Delta x_\beta = r\Delta x_\alpha$, where r is the volume expansion ratio due to the phase change. r has a value of 1.22 for the Sn-Li_2Sn_5 phase transformation. The finite difference grid used in the solution is shown in Fig. 4.

The simulation of the moving boundary starts with the initial Li concentration profile (Fig. 3) set to be the value calculated at the end of the nucleation period. In the numerical calculation, for a given time step j, the phase boundary S^j locates within the $i+1$ interval, which is between mesh points i and $i+1$. As the phase boundary propagate across the grids, the i and $i+1$ nodes will be updated accordingly.

By using the finite-difference method with the central difference in space and the forward Euler method in time, the discretized form of the diffusion equation seen in governing Equations g1 and g2 can be represented as

$$C_n^{j+1} = C_n^j + \frac{D_k \Delta t}{\Delta x_k^2}\left(C_{n-1}^j - 2C_n^j + C_{n+1}^j\right) \quad [9]$$

where superscript j denotes the time step, subscripts n and k denote the number of the mesh point and the phase (α or β) respectively. Δt is the size of time step and Δx is the grid spacing. For most of the nodal points, Eq. 9 can be used to calculate the Li concentration of a node in the next time step $j+1$ with the concentrations of the nearby nodes in time step j. The exceptions are the nodes at the electrolyte/anode interface, at the anode/substrate interface and the ones next to the moving phase boundary. For these nodes, the calculations are discussed below. In addition, since the phase boundary generally not located on a nodal point, the concentrations at the phase boundary need to be obtained separately as well.

The surface concentration is assumed to be a constant during the potentiostatic lithiation (boundary condition (b1)) so that C_S is a constant. The concentration of the node at anode/substrate interface is governed by boundary condition (b2). The condition is fulfilled by applying $C_{M-1}^j = C_{M+1}^j$, so Eq. 9 is modified to be

$$C_M^{j+1} = C_M^j + \frac{2D_\alpha \Delta t}{\Delta x_\alpha^2}\left(C_{M-1}^j - C_M^j\right). \quad [10]$$

The discretized boundary position at time step j is

$$S^j = \left(i + P^j\right)\Delta x_\beta \quad [11]$$

where P^j is a factor indicating the progression of phase boundary in the present $i+1$ interval which has a value between 0 and 1. Since the phase boundary is located between the i and $i+1$ nodes, the distances between the phase boundary and the two nodes are shorter than the grid spacings. Therefore, Lagrangian interpolation is performed to calculate the concentrations next to the phase boundary, C_i^{j+1} and C_{i+1}^{j+1}. The concentration at the i node in Li_2Sn_5 phase can be expressed as

$$C_i^{j+1} = C_i^j + \frac{2D_\beta \Delta t}{\Delta x_\beta^2}\left(\frac{C_{i-1}^j}{P^j+1} - \frac{C_i^j}{P^j} + \frac{C_{b^-}^j}{P^j\left(P^j+1\right)}\right) \quad [12]$$

where $C_{b^-}^j$ is the Li concentration at the phase boundary in Li_2Sn_5 phase. The concentration at the $i+1$ node in Sn phase is

$$C_{i+1}^{j+1} = C_{i+1}^j + \frac{2D_\alpha \Delta t}{\Delta x_\alpha^2}\left(\frac{C_{b^+}^j}{\left(1-P^j\right)\left(2-P^j\right)} - \frac{C_{i+1}^j}{1-P^j} + \frac{C_{i+2}^j}{2-P^j}\right) \quad [13]$$

where $C_{b^+}^j$ is the Li concentration at the phase boundary in Sn phase.

Following the same approach, Lagrangian interpolation is used to obtain the fluxes at the phase boundary, and the governing Equation g3 is represented as

$$D_\beta\left[\frac{1}{\Delta x_\beta}\left(\frac{P^j C_{i-1}^j}{P^j+1} - \frac{\left(P^j+1\right)C_i^j}{P^j} + \frac{\left(2P^j+1\right)C_{b^-}^j}{P^j\left(P^j+1\right)}\right)\right]\cdots$$
$$-D_\alpha\left[\frac{1}{\Delta x_\alpha}\left(\frac{\left(2P^j-3\right)C_{b^+}^j}{\left(1-P^j\right)\left(2-P^j\right)} + \frac{\left(2-P^j\right)C_{i+1}^j}{1-P^j} - \frac{\left(1-P^j\right)C_{i+2}^j}{2-P^j}\right)\right]$$
$$= \frac{\Delta x_\beta\left(C_{b^+}^j - C_{b^-}^j\right)}{\Delta t}\left(P^{j+1} - P^j\right). \quad [14]$$

As seen in boundary condition (b3), the concentrations across the phase boundary are related as

$$C_{b^+}^j = C_{\alpha\beta}^{eq} + \left(C_{b^-}^j - C_{\beta\alpha}^{eq}\right). \quad [15]$$

Therefore, the term $(C_{b^+}^j - C_{b^-}^j)$ in Eq. 14 can be simplified to a constant $(C_{\alpha\beta}^{eq} - C_{\beta\alpha}^{eq})$. In addition, by combing the boundary condition (b4) and Eq. 11, the position of the phase boundary in the next time step, P^{j+1}, is represented as

$$P^{j+1} = P^j + \frac{\Delta t}{\Delta x_\beta} K\left(C_{b^-}^j - C_{\beta\alpha}^{eq}\right). \quad [16]$$

Substituting Eqs. 15 and 16 back into Eq. 14, and rearranging the terms leads to a representation of $C_{b^-}^j$ as

$$C_{b^-}^{j}=\frac{\frac{D_\beta}{\Delta x_\beta}\left[\frac{P^j C_{i-1}^{j}}{P^j+1}-\frac{(P^j+1)C_i^j}{P^j}\right]-\frac{D_\alpha}{\Delta x_\alpha}\left[\frac{(2P^j-3)\left(C_{\alpha\beta}^{eq}-C_{\beta\alpha}^{eq}\right)}{(1-P^j)(2-P^j)}+\frac{(2-P^j)C_{i+1}^{j}}{1-P^j}-\frac{(1-P^j)C_{i+2}^{j}}{2-P^j}\right]+KC_{\beta\alpha}^{eq}\left(C_{\alpha\beta}^{eq}-C_{\beta\alpha}^{eq}\right)}{\frac{D_\alpha}{\Delta x_\alpha}\left[\frac{(2P^j-3)}{(1-P^j)(2-P^j)}\right]-\frac{D_\beta}{\Delta x_\beta}\left[\frac{(2P^j+1)}{P^j(P^j+1)}\right]+K\left(C_{\alpha\beta}^{eq}-C_{\beta\alpha}^{eq}\right)} \quad [17]$$

It is seen that the terms in Eq. 17 are all in the same time step. It can be used to solve the concentration at the phase boundary $C_{b^-}^{j}$ that can fulfill boundary condition at the interface with the other determined concentrations at the nearby nodes, i.e. *i-1*, *i*, *i+1* and *i+2* nodes. Therefore, Eq. 17 can be used to calculate $C_{b^-}^{j+1}$ if all the concentration at the nodes near the new position of the phase boundary in the next step *j+1* are known.

When $P^{j+1}<1$, the new phase boundary is still located in the current interval. A complete concentration profile can be obtain by applying Eqs. 9, 10, 12, 13, 17 and 15 sequentially.

On the other hand, if $P^{j+1}>1$, the phase boundary will move into the next interval in the next time step *j+1*, and the *i* and *i+1* nodes have to be re-defined, i.e. $i^{j+1}=i^j+1$. In this case, the concentration at the regular nodes can still be calculated by Eq. 9. However, the Eqs. 12 and 13 need to be modified to account for the migration of the phase boundary into the next grid interval. The concentration at nodes *i* and *i+1* are updated by Lagrangian interpolation according to

$$C_i^{j+1}=\frac{-P^{j+1}}{2+P^{j+1}}C_{i-2}^{j+1}+\frac{2P^{j+1}}{1+P^{j+1}}C_{i-1}^{j+1}+\frac{2}{\left(2+P^{j+1}\right)\left(1+P^{j+1}\right)}C_{b^-}^{j+1} \quad [18]$$

$$C_{i+1}^{j+1}=\frac{2}{\left(P^{j+1}-2\right)\left(P^{j+1}-3\right)}C_{b^+}^{j+1}+\frac{2-2P^{j+1}}{2-P^{j+1}}C_{i+2}^{j+1}+\frac{P^{j+1}-1}{3-P^{j+1}}C_{i+3}^{j+1} \quad [19]$$

which are substituted in Eq. 17. A new form of $C_{b^-}^{j+1}$ can be obtained and represented as

$$C_{b^-}^{j+1}=\frac{\frac{D_\beta}{\Delta x_\beta}\left[\frac{(P^{j+1}+1)C_{i-2}^{j+1}}{P^{j+1}+2}-\frac{(P^{j+1}+2)C_{i-1}^{j+1}}{P^{j+1}+1}\right]-\frac{D_\alpha}{\Delta x_\alpha}\left[\frac{(2P^{j+1}-3)\left(C_{\alpha\beta}^{eq}-C_{\beta\alpha}^{eq}\right)}{(1-P^{j+1})(2-P^{j+1})}+\frac{2\left(C_{\alpha\beta}^{eq}-C_{\beta\alpha}^{eq}\right)}{(1-P^{j+1})(3-P^{j+1})}+\frac{(3-P^{j+1})C_{i+2}^{j+1}}{2-P^{j+1}}+\frac{(P^{j+1}-2)C_{i+3}^{j+1}}{3-P^{j+1}}\right]+KC_{\beta\alpha}^{eq}\left(C_{\alpha\beta}^{eq}-C_{\beta\alpha}^{eq}\right)}{\frac{D_\alpha}{\Delta x_\alpha}\left[\frac{(2P^{j+1}-3)}{(1-P^{j+1})(2-P^{j+1})}+\frac{2}{(1-P^{j+1})(3-P^{j+1})}\right]-\frac{D_\beta}{\Delta x_\beta}\left[\frac{(2P^{j+1}+1)}{P^{j+1}(P^{j+1}+1)}-\frac{2}{P^{j+1}(P^{j+1}+2)}\right]+K\left(C_{\alpha\beta}^{eq}-C_{\beta\alpha}^{eq}\right)} \quad [20]$$

Lastly, the *P* factor is updated as $P^{j+1'}=P^{j+1}-1$ in Eq. 18 and Eq. 19 to get C_i^{j+1} and C_{i+1}^{j+1} and complete the concentration profile in the new time step *j+1*.

To validate this model, we compare the phase boundary evolution obtained by the numerical solution with an analytical solution of a semi-infinite film.[24] The analytical solution is solved for diffusion-controlled case and the thickness of the β phase S^{Analyt} is represented as

$$S^{Analyt}=\left[\left(\frac{Q^\beta R^{\beta 1}+R^{\beta 2}}{2}\right)^{1/2}-\frac{1}{2}\frac{1}{\sqrt{\pi}}\sqrt{\frac{D_\alpha}{D_\beta}}Q^\alpha R^\alpha\right]\left(4D_\beta t\right)^{1/2} \quad [21]$$

where *Q* and *R* are combinations of material constants. The details of the analytical solution are provided in Appendix A. As mentioned above, the phase propagation in the kinetic model is controlled by both diffusion and reaction happening at the phase boundary. Simulation results for the thickness of the β phase for several values of κ and the analytical solution for diffusion-controlled growth are shown in Fig. 5. κ is the normalized reaction rate coefficient and is represented as

$$\kappa=\frac{K}{K_o}\ \text{where}\ K_o=\frac{D_\beta}{\left(C_{\beta\alpha}^{eq}-C_{\alpha\beta}^{eq}\right)L_o}. \quad [22]$$

In order to compare with the semi-infinite analytical solution, we consider a system with a large value of thickness of α phase (9.25 μm) compared to the thickness of the β phase (< 150 nm). Note that the numerical solution starts with a finite thickness of the β phase equal to 40 nm as seen in Fig. 5. The values of parameters used in the calculations in Fig. 5 are presented in Table A1. In the simulation results, the reaction rate is controlled by the value of κ. Increasing κ changes the behavior of the phase boundary from interface-controlled to diffusion-controlled and the evolution of the β phase thickness changes from linear to parabolic with time. For large values of κ the numerical solution approaches the analytical result since the diffusion-controlled case corresponds to the limit of large reaction rate.

Calibration of numerical solution.—In the previous publication,[2] we discussed a characteristic current density profile (inset of Fig. 1a) at the beginning of potentiostatic lithiation and considered that feature to be due to the nucleation of the new phase. When the potential is changed to 0.65 V, a large current density appears, then decreases quickly followed by a gradual increase. The re-increase in current density is related to the nucleation of the Li_2Sn_5 phase at the surface. Once the nuclei of Li_2Sn_5 grow and form a continuous layer, the phase boundary initiates and the current density starts to decay. The elapsed time between the moment of potential change and the starting of the exponential decay is considered as the nucleation time, which was found to be approximately 1400 s in the experiment. The initial thickness of the lithiated phase S_o was estimated from the charge input during the nucleation time to be approximately 35 nm. According to the Li-Sn phase diagram, Li has very small solubility in Sn, below what can be measured reliably. However, the model requires the solubility as a parameter. The Li solubility in Sn phase $C_{\alpha\beta}^{eq}$ is assumed to be 5.0×10^{-25} mol/nm^3 (~0.01 Li atom per each Sn atom). The value has been used as one of the fitting parameters to get good agreement between the model and the experiments. These values are used in Eq. 5 to obtain the initial Li concentration profile.

A supporting experiment to show the effect of the nucleation period for the Li_2Sn_5 phase is shown in Fig. 6. First, the potential was held at 0.8 V for 20 hours to form the SEI before activating Sn-Li_2Sn_5 phase transformation. Subsequently, the potential was changed to 0.65 V for

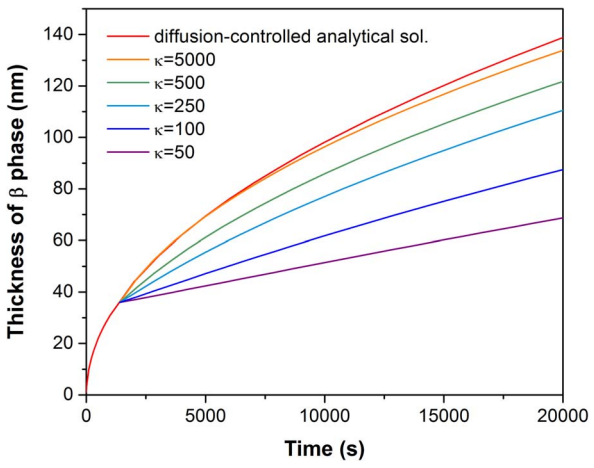

Figure 5. Comparison of the analytical solution for the semi-infinite diffusion-controlled case and numerical solutions for a 9.25 μm film with different values of normalized reaction rate coefficient κ.

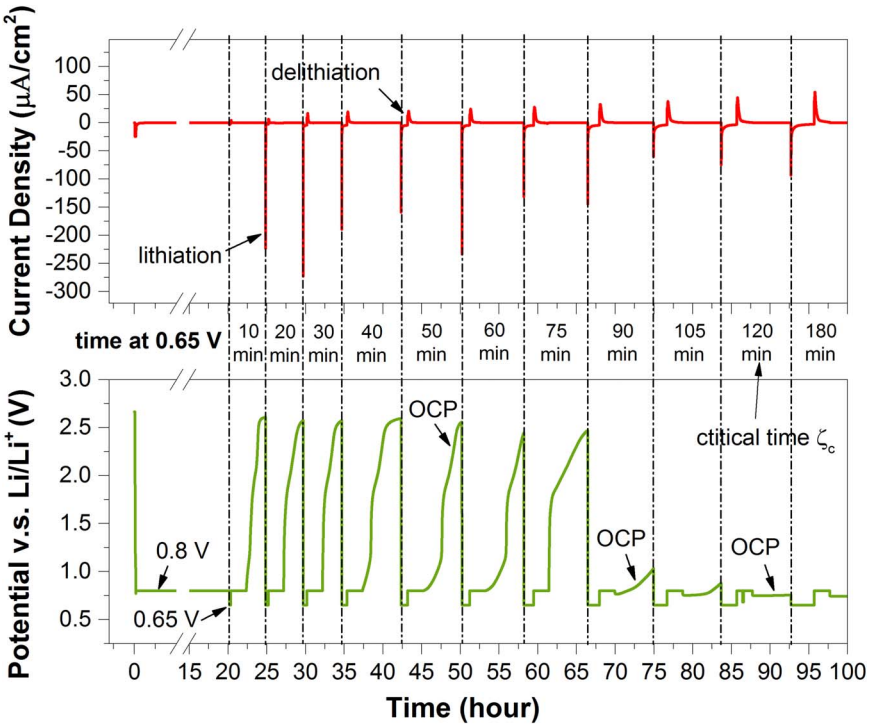

Figure 6. Experimental results underlying estimate of nucleation time for Sn-Li_2Sn_5 phase transformation.

different intervals of time and then raised to 0.8 V, followed by an open circuit potential (OCP) measurement to obtain the equilibrium surface potential. The cycle (0.65 V–0.8 V-OCP) was repeated with increasing lengths of elapsed time ζ at 0.65 V. When the potential is held at 0.65 V, the sample lithiates as seen from the current density profile (Fig. 6). The most significant observation in this experiment, as shown in Fig. 6, is that for a hold time ζ less than a critical time ζ_c, the OCP evolves to around 2.7 V, which is corresponding to the Sn phase, whereas for ζ greater than ζ_c, it evolves to a value below 1 V. During subsequent cycles, the OCP evolves to 0.76 V, which is the equilibrium potential of Li_2Sn_5 phase. Note that this transition in the open circuit potential response takes place abruptly. We attribute this transition to the nucleation of the Li_2Sn_5 phase from a supersaturated solid solution state. In this experiment, we found the critical time ζ_c to be approximately 120 minutes. Although the critical time ζ_c obtained from this experiment is not the same as seen in Fig. 1a, the difference in the experimental procedures (i.e. additional delithiation and OCP in the supporting experiment) possibly account for the discrepancy. The main conclusion from this supporting experiment is established that there is a finite nucleation time to begin formation of Li_2Sn_5 phase.

The kinetic parameters (D_α, D_β and K) are determined by using non-linear least square fitting to minimize the difference between the calculated Li flux and the measured current density. The resulting fit is shown in Fig. 1a. The C_s value was determined experimentally by performing a potentiostatic intermittent titration technique (PITT) experiment on a fully transformed Li_2Sn_5 layer; details are provided in the previous publication.[2] The parameters used in the simulation are provided in Table I, and the results of fitting parameters are presented in Table II.

Evolution of the simulated concentration profiles at different times are shown in Fig. 7. The sharp discontinuity in the concentration profiles indicates the evolving phase boundary position. The local Li concentration near the phase boundary in Li_2Sn_5 and Sn phases are shown in Figs. 8a and 8b respectively. The Li concentration in both phases are higher than the equilibrium concentrations. It is seen that the concentrations at the phase boundary approach to the equilibrium concentrations with progression of the phase boundary. Since the

Table I. Parameter values used in calibrations.

Initial thickness of anode, L_o	1850 nm
Number of node point, M	200
Grid spacing of Sn phase, Δx_α	9.25 nm
Grid spacing of Li_2Sn_5 phase, Δx_β	11.285 nm
Volume expansion ratio of Sn-Li_2Sn_5 phase transformation, r	1.22
Size of time step in simulation, Δt	0.072 s
Nucleation time of Sn-Li_2Sn_5 phase transformation, t_o	1400 s
Thickness of nucleation region, S_o	35 nm
Initial Li concentration in Sn phase, C_i	0 mol/nm^3
Stoichiometric Li concentration of Li_2Sn_5 phase	2.0590×10^{-23} mol/nm^3
(Equilibrium Li concentration in Li_2Sn_5 phase, $C^{eq}_{\beta\alpha}$)	(i.e. 0.4 Li atom per Sn atom)
Surface Li concentration in Li_2Sn_5 phase, C_S	2.0826×10^{-23} mol/nm^3
Biaxial modulus of fused-silica, M_S	86.4 GPa
Biaxial modulus of Sn, M_{Sn}	76.9 GPa
Thickness of fused-silica substrate, h_S	500 μm
Nominal yield stress of Sn, σ_o	−20 MPa
Low strain-rate yield stress of Li_2Sn_5, $\sigma_{Li_2Sn_5}$	−29 MPa
Stress-thickness of SEI, $\sigma_{SEI}h_{SEI}$	8.8 MPa-μm

Table II. Material parameters obtained by fitting.

Li solubility of Sn phase	5.0×10^{-25} mol/nm^3
(Equilibrium Li concentration in Sn phase, $C^{eq}_{\alpha\beta}$)	(i.e. ∼0.01 Li atom per Sn atom)
Li diffusivity in Sn phase, D_α	1.7×10^{-12} cm^2/s
Li diffusivity in Li_2Sn_5 phase, D_β	1.4×10^{-12} cm^2/s
Reaction coefficient of Sn-Li_2Sn_5 phase transformation, K	5.6×10^{-6} cm^4/mol s
Strain rate exponent, m	1.46
Strain rate coefficient, $\dot{\varepsilon}_o$	1.0×10^{-7}
Volume expansion of Sn phase due to Li insertion, η	9.47×10^{20} nm^3/mol

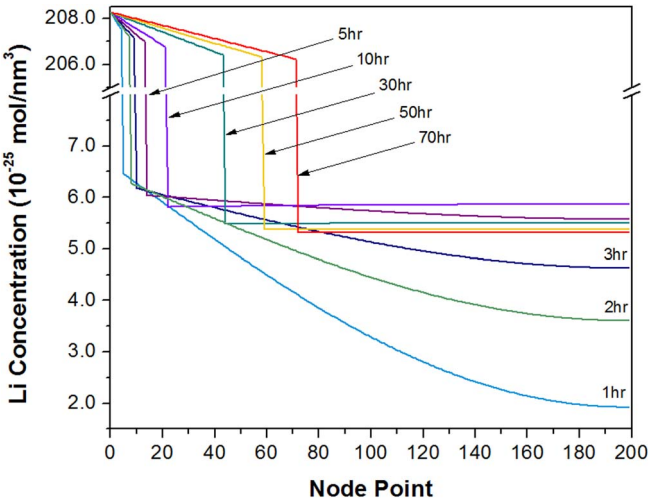

Figure 7. The calculated evolution of phase boundary and Li concentration profile in a Sn film with original thickness of 1.85 μm.

phase boundary velocity is determined by the supersaturation of Li at the phase boundary in Li_2Sn_5 phase (boundary condition b4), the decrease of the supersaturation leads to the slowing down of the phase boundary. Fig. 8a shows that the progression of the phase boundary position in each 10 hour interval becomes smaller for longer times of lithiation. In addition, Fig. 9 shows the comparison of the simulated thickness of Li_2Sn_5 and estimated values by considering the total charge accumulated at 0.65 V. An arrow in Fig. 9 indicates the starting point of the calculation. A good agreement is found indicating the simulation results for the phase boundary position is reasonable. It is seen that the growth of the Li_2Sn_5 phase is in a mixture of diffusion-controlled and interface-controlled kinetics.

Since the two concentrations at the phase boundary are coupled as seen in boundary condition (b3), a decrease in the supersaturation at the phase boundary in the Li_2Sn_5 phase leads to a decrease in the concentration on the other side of the interface as well. However, a more complicated evolution of the Li concentration in the Sn phase is seen in Fig. 8b. Since the Sn phase does not reach saturation during the nucleation period (the initial profile in Sn (Fig. 3) is not uniform), the high Li concentration at the phase boundary keeps driving Li into the Sn phase while the boundary moves forward, as seen in the concentration profiles in the Sn layer at 3 and 5 hours. The concentration in the Sn phase reaches saturation around 10 hours after the potential was lowered to 0.65 V. Subsequently, the concentration in the Sn layer starts to decrease to relax the excess Li above the Li solubility by diffusing toward the phase boundary and contributing to the phase transformation (which we refer to as flux reversal). As discussed below, the evolution of Li in the Sn induces a stress which causes the transient behavior observed in the curvature measurement.

Mechanism of stress evolution in Sn during lithiation.—The numerical solution provides a model for both the phase propagation and the Li concentration profile in the layers. Here we utilize these results to understand the evolution of the Li-induced stress distribution in the anode. As seen in the Fig. 8a, the concentration profile in the Li_2Sn_5 phase remains fairly linear during the interface propagation. Therefore, we assume the stress in the Li_2Sn_5 region remains at a constant low strain-rate yield stress. For the Sn phase, in previous work,[2] we reported that the Sn layer reaches the state of yield during the SEI formation period at 0.8 V before initiating Sn-Li_2Sn_5 phase transformation. As the concentration in the Sn layer evolves (Fig. 8b), two types of stress mechanisms are considered. First, as Li is driven into the Sn film, the rate-dependent stress is related to the strain rate of the Sn film. Here, we consider the film as an isotropic layer bonded to a rigid substrate, so the total strain rate in the lateral direction is constrained as

$$\dot{\varepsilon} = \dot{\varepsilon}^c + \dot{\varepsilon}^e + \dot{\varepsilon}^P = 0 \qquad [23]$$

where $\dot{\varepsilon}^c$ is the composition induced strain rate; $\dot{\varepsilon}^e$ is the elastic strain rate, and $\dot{\varepsilon}^P$ is the plastic strain rate.

For an isotropic continuum, the in-plane composition strain rate $\dot{\varepsilon}^c$ can be related to the volumetric strain rate $\dot{\varepsilon}^c_V$ as

$$\dot{\varepsilon}^c = \frac{1}{3}\dot{\varepsilon}^c_V = \frac{1}{3}\,\eta\dot{C} \qquad [24]$$

where η is the volume expansion of Sn due to Li insertion and $\dot{C}$ is the rate of Li concentration change.

Under the thin film configuration, the in-plane elastic strain rate can be represented as

$$\dot{\varepsilon}^e = \frac{\dot{\sigma}_{Sn}}{M_{Sn}} = \frac{1}{M_{Sn}}\frac{d\sigma_{Sn}}{dt} \qquad [25]$$

where M_{Sn} is the biaxial modulus of Sn. In the stress measurement (Fig. 1b), the stress-thickness of the micron-level Sn film indicates the stress is in the MPa range, whereas the biaxial modulus of Sn is in the GPa range. In addition, the change of stress in the measurement

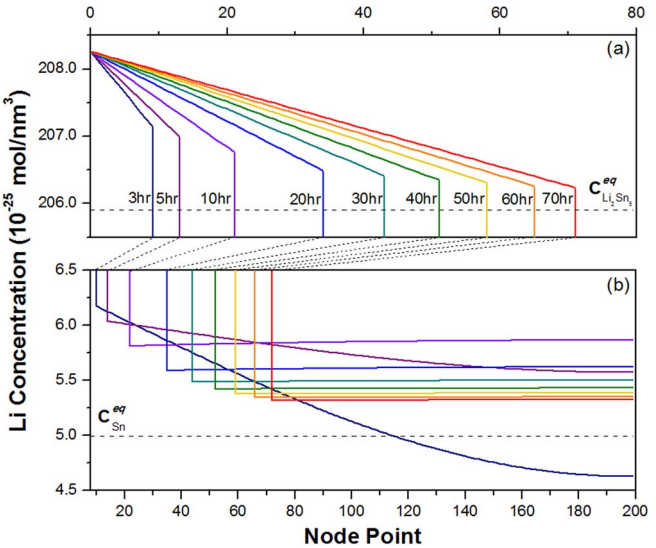

Figure 8. The calculated evolution of Li concentration profile near the phase boundary. (a) in Li_2Sn_5 phase; (b) in Sn phase.

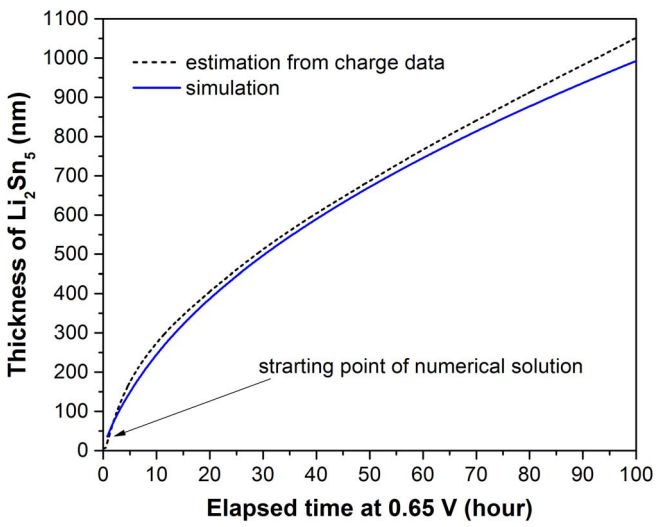

Figure 9. Comparison of the calculated thickness of Li_2Sn_5 phase and the estimation from the charge data. The arrow indicates the starting thickness of Li_2Sn_5 in finite-difference calculation.

happens in several hours. Therefore, we assume $\dot{\varepsilon}^e$ is negligible in this case.

For the plastic strain rate, we assume it can be described by viscoplasticity[25] as

$$\dot{\varepsilon}_{ij}^P = \dot{\varepsilon}_o \left[\left(\frac{\sigma_e}{\sigma_o} \right)^m - 1 \right] \frac{3}{2} \frac{S_{ij}}{\sigma_e} \quad [26]$$

where $\dot{\varepsilon}_o$ is the strain rate constant; m is the strain rate exponent; σ_o is the nominal yield stress and it is assumed to be a constant. S_{ij} is the deviatoric stress and σ_e is the von Mises stress: $\sigma_e = \sqrt{\frac{3}{2} S_{ij} S_{ij}}$. In the thin film case, the components of deviatoric stress are: $S_{11} = S_{22} = \sigma_{Sn}/3$ and $S_{33} = -2\sigma_{Sn}/3$, and $\sigma_e = |\sigma_{Sn}|$. These results lead to the in-plane plastic strain rate as

$$\dot{\varepsilon}^P = \dot{\varepsilon}_{11}^P = \dot{\varepsilon}_{22}^P = \frac{\dot{\varepsilon}_o}{2} \left[\left(\frac{|\sigma_{Sn}|}{\sigma_o} \right)^m - 1 \right]. \quad [27]$$

Since the $\dot{\varepsilon}^e$ is assumed to be negligible, by substituting $\dot{\varepsilon}^e$, $\dot{\varepsilon}^P$ and applying Eq. 23, the rate-dependent stress in the Sn film is represented as

$$\sigma_{Sn} = \sigma_o \left(\frac{2\eta}{3\dot{\varepsilon}_o} \dot{C} + 1 \right)^{\frac{1}{m}}. \quad [28]$$

When the rate of the concentration change $\dot{C}$ is large and positive, the associated volume expansion leads to a large strain rate and thus a large transient stress as seen in Fig. 1b. Further discussion of the rate-dependent stress and the effect of the parameters in Eq. 28 on the stress evolution is provided in Appendix B.

There is also a second mechanism that can contribute to the transient stress response. When the phase boundary nucleates and begins to propagate, the Li flux in the supersaturated Sn phase can reverse its direction and flow toward the phase boundary. Such a reversal leads to elastic unloading of the Sn phase due to a decrease in volume. The relaxation of the transient stress response would be due to a combination of decreasing rate of concentration change and elastic unloading. The stress state of the elastic unloading can be described as

$$\sigma_{Sn} = \sigma_{Sn}^{ul} - B\Delta C^{ul} \quad [29]$$

where $B = \eta M_{Sn}$ for the thin film geometry. σ_{Sn}^{ul} is the local stress in Sn right before elastic unloading; it is a function of position x and its magnitude is given by Eq. 28. ΔC^{ul} is the local decrease of concentration during elastic unloading. This mechanism causes the stress in Sn to be reduced from the stress produced by the plastic deformation. Note that the two mechanisms may happen at different positions in the Sn phase at the same time, e.g. elastic unloading can start happening in a region near the phase boundary while the interior of the layer remains at the state of yield.

Fig. 10 shows a schematic plot to demonstrate the correlation between the evolution of Li concentration and the corresponding stress for the 2-phase system being investigated here. In Fig. 10a, two calculated Li concentration profiles (at time step t and its preceding time step *t-1*) are presented. It is seen that as the phase boundary propagates from S(t-1) to S(t), the Li concentrations in the Sn phase at the phase boundary decreases (which is also seen in Figs. 7 and 8b). Such evolution leads to the two overlapping concentration profiles in the Sn phase shown in the figure. The point where the two profiles have the same concentration is labeled as "flux-reversal boundary" in Fig. 10a; the directions of the Li flux on either side of it are in opposite directions as shown by the arrows in light blue. Depending on the direction of Li flux (i.e. the sign of $\dot{C}$), the corresponding stress in Sn at time t (Fig. 10b) can be determined using the mechanisms discussed above. As mentioned earlier, the concentration profile in the Li_2Sn_5 phase is linear and the stress is assumed to be at a constant low strain-rate yield stress $\sigma_{Li_2Sn_5}$. For the Sn phase region beyond the flux-reversal boundary, the Li concentration increases from time *t-1* to time t (i.e. $\dot{C} > 0$), and the higher stress state is due to the rate-dependent plasticity (i.e. viscoplasticity) associated with the strain rate induced by the increasing Li concentration (Eq. 28). For the Sn phase region close

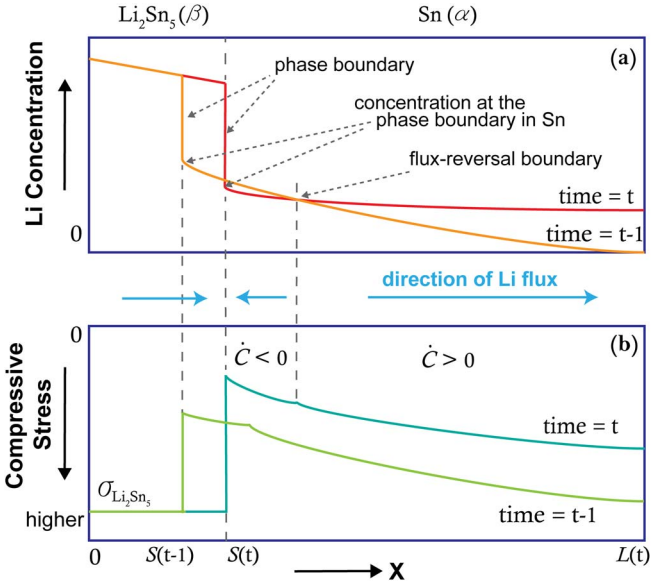

Figure 10. Schematic plot of (a) Li concentration profiles at time t and t-1 showing the flux-reversal boundary induced by the phase boundary propagation; (b) the stress distribution at time t corresponding to the evolution in (a) and the preceding stress distribution at time t-1.

to the phase boundary, the Li concentration decreases from time *t-1* to time t (i.e. $\dot{C} < 0$), in which the stress decreases from its rate-dependent stress (elastic unloading, Eq. 29) due to the reversed Li flux from Sn to the phase boundary. Similarly, the stress distribution at time *t-1* shown in Fig. 10b (or other time steps) can be obtained from the corresponding Li concentration profiles at the preceding times.

Calculation of stress evolution in Sn.—In the numerical solution, the rate of concentration change at each nodal point n in a given time step can be calculated from the concentrations in that and the preceding time steps, which can be expressed as

$$\dot{C}_n^{j+1} = \frac{C_n^{j+1} - C_n^j}{\Delta t} \quad [30]$$

For nodal points that have positive sign $\dot{C}_n^{j+1}$, the states of stress are determined by Eq. 28. In contrast, if the sign is negative, the stress is determined by Eq. 29. Sequentially, an integral of stress with thickness is performed to have the stress-thickness value that can be used to compare with the measured values in the experiment.

In the previous work,[2] we reported that the low strain-rate yield stress of Li_2Sn_5 is around -29 MPa. We also observed the tensile contribution with a value of 8.8 MPa-μm from the SEI at the anode surface. Here, we use the information obtained previously from the steady state and the diffusion profile by numerical solution to analyze the transient state. The elastic modulus and Poisson's ratio of Sn reported by Stournara et al.[26] and the material parameters applied in the calibration are shown in Table I.

The calculated stress distribution in the anode is shown in Fig. 11 for different times indicated on the figure. The regions where the different stress mechanisms activate are distinguished by the arrows labeled "flux-reversal boundary" in each stress profile. As discussed above, the stress in the regions of Sn far away from the phase boundary (distances greater than indicated by the arrows) is at a higher stress state governed by viscoplasticity (Eq. 28). Near the phase boundary (distances less than the arrows), the stress decreases from its rate-dependent stress as described by elastic unloading (Eq. 29). The integrated stress-thickness of the entire anode is used to fit the model to the values measured by wafer curvature and calibrate the mechanical parameters used in Eqs. 28 and 29. The fitting result is shown in Fig. 1b, in which the solid line corresponds to experimental data and the

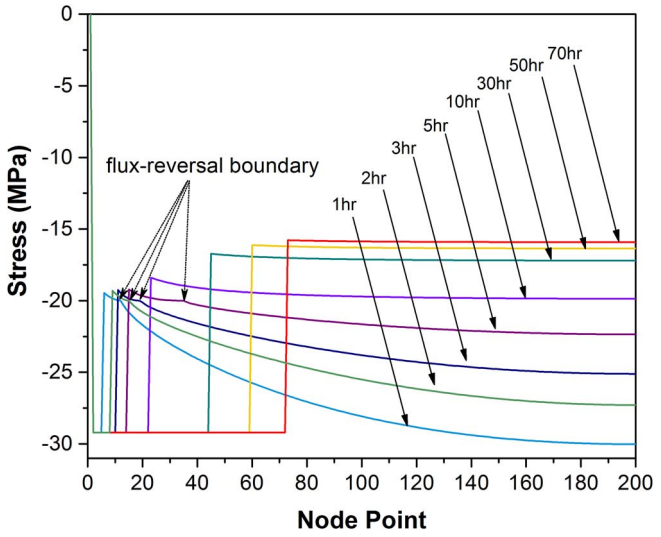

Figure 11. The calculated evolution of stress distribution in Sn film with original thickness of 1.85 μm.

dash line corresponds to the simulation result. The points marked by arrows correspond to the concentration profile in Fig. 7 and Fig. 8 and the stress profile in Fig. 11 at the corresponding times. The results of calibrated parameters are presented in Table II.

According to the results in Figs. 1b and 11, the stress in Sn induced by Li diffusion leads to a stress state above the nominal yield stress at the beginning of the phase transformation. At this stage, the contribution to the stress-thickness from the Li_2Sn_5 phase is smaller than the Sn phase since the majority of the anode remains in the Sn phase. Therefore, the high stress-thickness in the transient behavior is mostly the result of rate-dependent stress in Sn. Subsequently, as the excess Li concentration in the Sn layer approaches saturation, the decrease in the rate of concentration change relaxes the high stress state in Sn (1–5 hours at region greater than the flux reversal boundary in Fig. 11), so that the high stress-thickness value of the anode is eased. The decrease in the excess Li concentration leads to a lower stress state in Sn by elastic unloading (the entire Sn region beyond 10 hour in Fig. 11). A balance between the high stress in Li_2Sn_5 and the lower stress in Sn leads to the fairly constant value of stress-thickness between 10 and 30 hours (Fig. 1b). As the Sn/Li_2Sn_5 phase boundary propagates in Sn, the stress-thickness reaches a steady rate of increase as the contribution from Li_2Sn_5 phase becomes dominant and the stress in Sn reaches a steady state value.

Conclusions

In this paper, we studied the large transient stress observed at the beginning of the Sn-Li_2Sn_5 phase transformation. We performed a numerical simulation to solve the 1-D moving boundary problem of the Li_2Sn_5 phase growing into the parent Sn phase during potentiostatic lithiation. Using the calculated Li concentration profiles, we proposed mechanisms for the observed stress evolution in Sn. The kinetic and mechanical parameters were calibrated with the experimental measurements. The main conclusions of this study are:

- The results of the phase kinetic modeling indicates that the Li diffusivity in Sn and Li_2Sn_5 are approximately 10^{-12} cm^2/s, and the reaction rate coefficient is approximately 5×10^{-6} cm^4/mol s. The results obtained by the numerical solution are consistent with the values found in the previous steady-state analysis.[2]
- The high value of stress-thickness of the transient behavior at the beginning of Sn-Li_2Sn_5 phase transformation is induced by rate-dependent plasticity associated with the excess Li diffusion in Sn layer.
- As the phase boundary propagates, the flux of Li diffusion decreases and the relaxation of the excess Li concentration leads to a lower state of stress in Sn by elastic unloading. The balance between the region of elastic unloading and the growing new phase result in a period of approximate constant stress-thickness. Subsequently, it begins to increase at a steady rate as the new phase continues to grow.

The modeling and analysis method developed here may can be extended to other material systems to study phase transformation problems and future research on the failure mechanisms of the battery electrodes.

Acknowledgments

The authors gratefully acknowledge Professor Allan F. Bower for the valuable discussions of the manuscript, and the support by the Experimental Program to Stimulate Competitive Research (EPSCoR) sponsored by United States Department of Energy under grant DE-SC0007074.

Appendix A

The analytical solution of the diffusion-controlled case of a semi-infinite film is provided by R. F. Sekerka and S.-L. Wang in a chapter of a book Lectures of the Theory of Phase Transformations by H. Aaronson.[24] The solution was developed from the typical form of error function for the infinite spatial domain. To modify the solution for semi-infinite case, the surface is treated as another interface. Therefore, in this analytical solution, there are two moving interfaces. One is phase boundary ξ_1 between α and β phases; another is the surface ξ_2. The difference between ξ_1 and ξ_2 is the thickness of the new β phase that forms.

$$\xi_1 - \xi_2 = \left[\left(\frac{Q^\beta R^{\beta 1} + R^{\beta 2}}{2} \right)^{1/2} - \frac{1}{2} \frac{1}{\sqrt{\pi}} \sqrt{\frac{D_\alpha}{D_\beta}} Q^\alpha R^\alpha \right] \sqrt{4 D_\beta t} \qquad [A1]$$

where Q and R are combinations of material constants as shown below:

$$R^\alpha = \frac{C_B^{\alpha\beta} - C_B^{\alpha\infty}}{C_B^{\beta\alpha} - C_B^{\alpha\beta}}, R^{\beta 1} = \frac{C_B^{\beta\xi} - C_B^{\beta\alpha}}{C_B^{\beta\alpha} - C_B^{\alpha\beta}}, R^{\beta 2} = \frac{\bar{V}_B^\beta \left(C_B^{\beta\xi} - C_B^{\beta\alpha} \right)}{1 - \bar{V}_B^\beta C_B^{\beta\xi}}$$

$$Q^\alpha = \frac{1}{\bar{V}_A^\alpha \Delta}, Q^\beta = \frac{\bar{V}_A^\beta C_A^{\alpha\beta} + \bar{V}_B^\beta C_B^{\alpha\beta}}{\bar{V}_B^\beta \Delta}, \Delta = \frac{C_B^{\beta\alpha} C_A^{\alpha\beta} - C_B^{\alpha\beta} C_A^{\beta\alpha}}{C_B^{\beta\alpha} - C_B^{\alpha\beta}}$$

Eq. A1 is the form we used for calculating the analytical solution and to use in comparison with the numerical solution. In the case discussed in this paper, α phase is

Table A1. Parameters used in the simulation in Fig. 5.

Assigned Li diffusivity in Sn phase, D_α	3×10^{-13} cm^2/s
Assigned Li diffusivity in Li_2Sn_5 phase, D_β	4×10^{-13} cm^2/s
Li concentration at the surface in Li_2Sn_5 phase, $C_B^{\beta\xi}$	2.0826×10^{-23} mol/nm^3
Li concentration at the interface in Li_2Sn_5 phase, $C_B^{\beta\alpha}$	2.0590×10^{-23} mol/nm^3*
Li concentration at the interface in Sn phase, $C_B^{\alpha\beta}$	5.0×10^{-25} mol/nm^3
Li concentration at infinity in Sn phase, $C_B^{\alpha\infty}$	0 mol/nm^3
Sn concentration at the interface in Li_2Sn_5 phase, $C_A^{\beta\alpha}$	5.1475×10^{-23} mol/nm^3*
Sn concentration at the interface in Sn phase, $C_A^{\alpha\beta}$	6.1410×10^{-23} mol/nm^3*
Partial molar volume of Sn in Sn phase, $\bar{V}_A^\alpha$	1.63×10^{22} nm^3/mol*
Partial molar volume of Sn in Li_2Sn_5 phase, $\bar{V}_A^\beta$	1.67×10^{22} nm^3/mol*
Partial molar volume of Li in Li_2Sn_5 phase, $\bar{V}_B^\beta$	7.92×10^{21} nm^3/mol*

*Values calculated with the theoretical densities reported in Ref. 11.

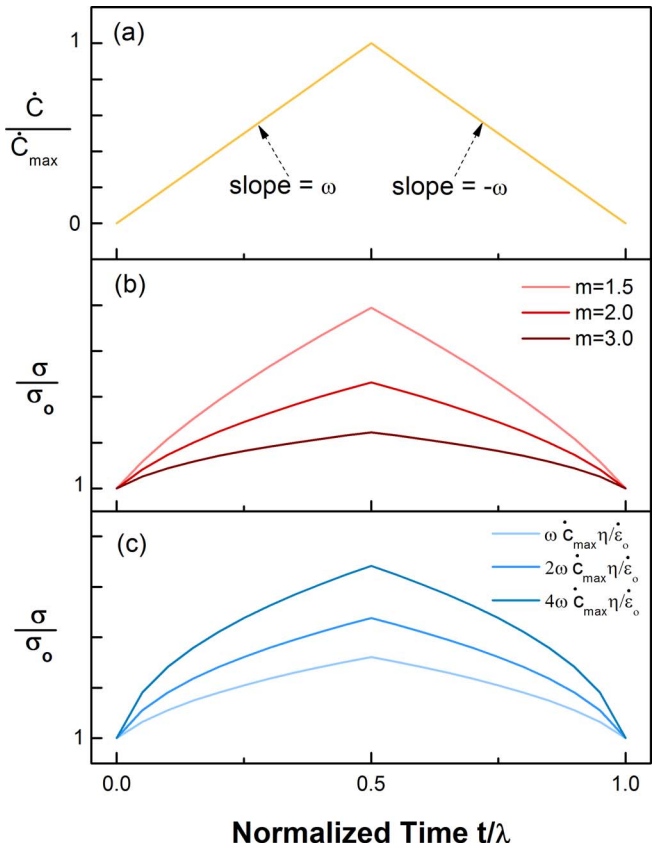

Figure B1. Demonstration of the correlation between rate-dependent stress and the material parameters. (a) normalized rate of concentration change $\frac{\dot{C}}{\dot{C}_{max}}$; (b) and (c): trends of the normalized rate-dependent stress $\frac{\sigma}{\sigma_o}$ with parameters m and $\frac{\eta}{\dot{\varepsilon}_o}\omega\dot{C}_{max}$ respectively.

Sn; β phase is Li_2Sn_5 phase, and element A is Sn atom; element B is Li atom. $\bar{V}$ terms are partial molar volumes, and the values are estimated by considering linear volume expansion between phases.

Appendix B

The rate-dependent stress response of lithiated Sn phase is assumed to be described with the following viscoplastic model

$$\frac{\sigma}{\sigma_o} = \left(\frac{2\eta}{3\dot{\varepsilon}_o}\dot{C} + 1\right)^{\frac{1}{m}} \quad [B1]$$

where $\frac{\sigma}{\sigma_o}$ is the normalized rate-dependent stress; η is the volume expansion induced by Li insertion; $\dot{\varepsilon}_o$ is the strain rate constant; m is the strain rate exponent, and $\dot{C}$ is the rate of concentration change. The objective of this appendix is to illustrate the influence of the parameters on the induced stress. This is done by assuming a bilinear change in $\dot{C}$ as shown Fig. B1a. It should be noted that the actual $\dot{C}$ in the experiment is determined by the experimental condition and the kinetic parameters of the system. The assumed variation of $\dot{C}$ in Fig. B1a is chosen for illustration purpose only.

In Fig. B1a, $\dot{C}$ can be normalized with its maximum value $\dot{C}_{max}$, and the normalized rate of concentration $\frac{\dot{C}}{\dot{C}_{max}}$ can be represented as

$$\frac{\dot{C}}{\dot{C}_{max}} = \omega\frac{t}{\lambda} \quad [B2]$$

where $\frac{t}{\lambda}$ is the normalized time, and λ is total length of time t; ω is the slope of $\frac{\dot{C}}{\dot{C}_{max}}$ and $\frac{t}{\lambda}$, i.e. the second derivative with respect to time. The slope ω depends on the experiment condition and may alter during the experiment. Fig. B1a shows an example of $\frac{\dot{C}}{\dot{C}_{max}}$ versus $\frac{t}{\lambda}$ with a constant slope ω, in which $\frac{\dot{C}}{\dot{C}_{max}}$ is assumed to start increasing linearly to 1 as the normalized time $\frac{t}{\lambda}$ reaches 0.5, and then decrease linearly (note that $\omega = 2$ in Fig. B1a). Eq. B2 can used to describe the first segment of $\frac{\dot{C}}{\dot{C}_{max}}$ in Fig. B1a, where the slope ω is positive, and the rate-dependent stress shown in Eq. B1 can be normalized as

$$\frac{\sigma}{\sigma_o} = \left(\frac{2\eta}{3\dot{\varepsilon}_o}\omega\dot{C}_{max}\frac{t}{\lambda} + 1\right)^{\frac{1}{m}}. \quad [B3]$$

It is seen that the magnitude of $\frac{\sigma}{\sigma_o}$ depends on the values of m and $\frac{\eta}{\dot{\varepsilon}_o}\omega\dot{C}_{max}$. The strain rate exponent, the volume expansion associated with Li insertion η and the strain rate constant $\dot{\varepsilon}_o$ are material properties, whereas the product $\omega\dot{C}_{max}$ is related to the Li diffusivity in the material, and can vary with experimental conditions. A similar expression for the decreasing portion of Fig. B1a, which is not shown for brevity.

To illustrate the influence of the parameters m and $\frac{\eta}{\dot{\varepsilon}_o}\omega\dot{C}_{max}$ on the normalized rate-dependent stress, Figs. B1b and B1c show calculations of $\frac{\sigma}{\sigma_o}$ for different values of m and $\frac{\eta}{\dot{\varepsilon}_o}\omega\dot{C}_{max}$, respectively, with the values indicated in the figures. It can be seen that when $\frac{\dot{C}}{\dot{C}_{max}}$ is positive and large, it leads to a high rate-dependent stress. In contrast, when $\frac{\dot{C}}{\dot{C}_{max}}$ is positive but small, $\frac{\sigma}{\sigma_o}$ approaches 1 as the rate-dependent stress approaches the nominal yield stress. As shown in Fig. B1b, for smaller values of m, $\frac{\sigma}{\sigma_o}$ is more sensitive to $\frac{\dot{C}}{\dot{C}_{max}}$ and results in a larger magnitude of $\frac{\sigma}{\sigma_o}$. The parameters $\frac{\eta}{\dot{\varepsilon}_o}$ and $\omega\dot{C}_{max}$ influence stress evolution through the non-dimensional group $\frac{\eta}{\dot{\varepsilon}_o}\omega\dot{C}_{max}$, which is illustrated in Fig. B1c. Higher volume expansion coefficient η and higher lithiation rate $\omega\dot{C}_{max}$ lead to higher stress as expected.

References

1. I. Rom, M. Wachtler, I. Papst, M. Schmied, J. O. Besenhard, F. Hofer, and M. Winter, *Solid State Ionics*, **143**, 329 (2001).
2. C.-H. Chen, E. Chason, and P. R. Guduru, *Journal of Electrochemical Society*, **164**(4), A574 (2017).
3. A. F. Bower and P. R. Guduru, *Modelling Simul. Mater. Sci. Eng.*, **20**, 045004 (2012).
4. J. Zhang, B. Lu, Y. Song, and X. Ji, *Journal of Power Sources*, **209**, 220 (2012).
5. J. Christensen, *Journal of The Electrochemical Society*, **157**(3), A366 (2010).
6. T. G. Myers and S. L. Mitchell, *Applied Mathmetical Modeling*, **35**, 4281 (2011).
7. L. I. Rubinshteĭn, *The Stefan Problem*, American Mathematical Soc. (1971).
8. Z. Cui, F. Gao, and J. Qu, *Journal of the Mechanics and Physics of Solids*, **61**, 293 (2013).
9. A. Singer, A. Ulvestad, H.-M. Cho, J. W. Kim, J. Maser, R. Harder, Y. S. Meng, and O. G. Shpyrko, *Nano Letter*, **14**(9), 5295 (2014).
10. S. Hulikal, C.-H. Chen, E. Chason, and A. Bower, *Journal of Electrochemical Society*, **163**(13), A2647 (2016).
11. M. Winter and J. O. Besenhard, *Electrochimica Acta*, **45**, 31 (1999).
12. A. V. Virkar, *Journal of Power Sources*, **147**(1–2), 8 (2005).
13. M. Hillert, in *Lectures on the Theory of Phase Transformations*, H. I. Aaronson, ed., The Minerals, Metals & Materials Society, (1999).
14. W. G. Moffatt, *The Handbook of Binary Phase Diagrams*, Schenectady, N.Y. (1978).
15. J. Svoboda, F. D. Fischer, P. Fratzl, E. Gamsjager, and N. K. Simha, *Acta Materialia*, **49**, 1249 (2001).
16. J. Sietsma and S. v. d. Zwaag, *Acta Materialia*, **52**, 4143 (2004).
17. J. Crank and R. S. Gupta, *IMA Journal of Applied Mathematics*, **10**(1), 19 (1972).
18. B. Chao, S.-H. Chae, X. Zhang, K.-H. Lu, M. Ding, J. Im, and P. S. Ho, *Journal of Applied Physics*, **100**, 084909 (2006).
19. J. W. Cahn and J. E. Hilliard, *American Institute of Physics*, **31**, 688 (1959).
20. J. W. D. Connolly and A. R. Williams, *Physical Review B*, **27**(8), 5169 (1983).
21. H. Ji, D. Chopp, and J. E. Dolbow, *International Journal for Numerical Methods in Engineering*, **54**(8), 1209 (2002).
22. M. Hillert, *Metallurgical Transactions A*, **6**(1), 5 (1975).
23. J. Crank, *Free and Moving Boundary Problems*, Oxford (1984).
24. R. F. Sekerka and S.-L. Wang, in *Lectures on the Theory of Phase Transformations*, H. I. Aaronson, ed., The Minerals, Metals & Materials Society, (1999).
25. A. F. Bower, *Applied Mechanics of Solids*, CRC Press (2009).
26. M. Stournara, P. R. Guduru, and V. Shenoy, *Journal of Power Sources*, **208**, 165 (2012).